Journal of Materials Chemistry B

ROYAL SOCIETY OF CHEMISTRY

PAPER

View Article Online
View Journal | View Issue

Check for updates

Cite this: J. Mater. Chem. B, 2025, 13, 11439

3D printable PCL-*b*-P(MMA-*co*-TMSPMA)/silica hybrids using a PCL RAFT agent

Athanasios Skandalis,[a] Haffsah Iqbal,[a] Gloria Young,[a] David R. Sory,[b] Jingwen Liu,[c] Peter D. Lee,[c] Sara M. Rankin,[b] Theoni K. Georgiou[a] and Julian R. Jones*[a]

Inorganic/organic hybrid biomaterials have the potential to combine the benefits of bioactive glasses, such as bone bonding and osteogenesis, with the ability to withstand cyclic loading. Here, we report on silica/poly(ε-caprolactone-methacrylate) hybrids, using hydroxy monofunctional-PCL as a reversible addition–fragmentation chain transfer (RAFT) agent, for controlled polymerization of PCL-*b*-P(methyl methacrylate-*co*-3-(trimethoxysilyl)propyl methacrylate), PCL-*b*-P(MMA-*co*-TMSPMA), block copolymers by a combination of ring opening polymerization (ROP) and RAFT polymerization techniques. The new polymer was used for the preparation of hybrids *via* the sol–gel method, with TMSPMA providing covalent bonds between the silica and PCL-*b*-P(MMA-*co*-TMSPMA). The effect of the ratio of CL/silane containing units on the mechanical properties of the hybrids was investigated. The compositions that yielded optimal mechanical properties in bulk form (yield stress 39.3 MPa to 52.9 MPa at a strain of 4–6%) were developed into "inks" for 3D printing porous biodegradable scaffolds for biomedical applications by direct writing. Degradation tests of scaffolds in phosphate buffered saline (PBS) over the course of 180 days showed ~30% degradation of PCL. The mechanical properties of scaffolds with pore channels of 234–380 μm reduced yield strength to 5.2–7.4 MPa, but yield strain remained at ~4%. *In vitro* studies indicated biocompatibility, in terms of exposure of human bone marrow stem cells (hBMCs) to the dissolution products of the scaffolds.

Received 31st January 2025,
Accepted 9th August 2025

DOI: 10.1039/d5tb00220f

rsc.li/materials-b

Open Access Article. Published on 27 August 2025. Downloaded on 10/3/2025 4:51:24 PM.
This article is licensed under a Creative Commons Attribution 3.0 Unported Licence.

Introduction

There is unmet clinical need for synthetic bone graft materials that can stimulate bone regeneration and share cyclic loads with the host bone. Silica based bioactive glasses can bond with bone and promote osteogenesis through ion (silica species and calcium ions) release but are brittle.[1] Inorganic–organic sol–gel hybrids are composed of co-networks of organic and inorganic segments that interact at the molecular level and can be engineered to match the mechanical properties of the surrounding bone more closely than bioactive glasses, potentially offering better support and stability in the regenerated area.[2–6] There are several options for the organic component. If the material is to be biodegradable, a biodegradable polymer should be chosen.

The inorganic component is usually based on silica (SiO_2) to retain the bioactive properties of bioactive glass,[7,8] and to act as a rigid network that provides compressive strength. Covalent bonding between the organic and inorganic networks is needed to prevent premature dissolution of the hybrid. This can be achieved by incorporating silane-functionalized blocks into co-polymer chains.[6]

One strategy for obtaining the covalent bonding is to use a coupling agent, functionalizing the polymer before addition to the sol–gel process (class II hybrid). Early examples include use of synthetic biodegradable polymers, such as poly(ε-caprolactone)-diol, using isocyanatopropyl triethoxysilane (IPTS) as the coupling agent,[9,10] with the cyanate group reacting with the terminal hydroxyl groups of the PCL chains. PCL hybrids with 60 wt% PCL (M_w 6700 Da) had a tensile strength of 21 MPa. Further tailoring of the properties was limited by the coupling site which was only at the ends of the polymer chains.

Pendant functional groups along polymer chains are naturally present in biopolymers, such as chitosan,[11–14] gelatin[15–17] and poly(γ-glutamic acid)[18,19] and can be coupled using glycidoxypropyltrimethoxysilane (GPTMS). Polymer functionalization can occur by nucleophiles, such as carboxylic acid groups, opening the epoxy ring of the GPTMS.[20,21] While the mechanical properties and degradation was tailorable through the amount of GPTMS used, the reaction was difficult to control. Recently, hybrids made by reacting PCL-diCOOH with GTPMS in tetrahydrofuran (THF) led to a class IV hybrid, whereby the

[a] Department of Materials, Imperial College London, SW7 2AZ, London, UK. E-mail: julian.r.jones@imperial.ac.uk
[b] National Heart & Lung Institute, Faculty of Medicine, Imperial College London, SW7 2AZ, London, UK
[c] Department of Mechanical Engineering, University College London, London, UK

Open Access Article. Published on 27 August 2025. Downloaded on 10/3/2025 4:51:24 PM.
This article is licensed under a Creative Commons Attribution 3.0 Unported Licence.

THF was involved in cationic ring opening polymerization to produce a SiO_2/PCL-COOH/pTHF hybrid with excellent mechanical properties.[22]

Copolymers of methyl methacrylate (MMA) and 3-(trimethoxysilyl)propyl methacrylate (TMSPMA) have been used to the organic and silica co-network,[23,24] with the TMSPMA binding to the silicate network, which showed biocompatibility *in vivo* and *in vitro*.[25–28] The poly(MMA-*co*-TMSPMA) copolymers can be synthesized with different architectures, *e.g.* star polymer architectures, within which the arms and cross-linking core can be modified independently.[29–33]

As methacrylates are not biodegradable, they cannot be used to make fully degradable hybrid materials, but biodegradable linkages can be incorporated so they can be cleaved *in vivo*, leaving non degradable segments. The molar mass (MM) of such segments should be less than approximately 30 kg mol^{-1} to pass through the glomeruli pores in kidneys. Careful control of MM can be achieved through controlled polymerization methodologies (*e.g.* RAFT).[34–36]

To produce scaffolds for bone regeneration, hybrid sols can be 3D printed by direct ink writing, with pore channels in excess of 100 μm.[22,37] An example is poly(MMA-*co*-TMSPMA)-*star*-SiO_2 hybrid formulations. The star polymers consisted of linear poly(MMA-*co*-TMSPMA) arms with a molar ratio of MMA_{100}-$TMSPMA_{10}$ linked with an ethylene glycol dimethacrylate (EGDMA) core.[38] Similar hybrid systems were also produced with a peptide core designed to degrade on exposure to specific enzymes.[33]

Here, we use PCL as the degradable segments of PCL-*b*-P(MMA-*co*-TMSPMA) block copolymers. The copolymers were prepared by a combination of ROP and RAFT polymerization techniques, using PCL RAFT agents,[39,40] and were utilized for the preparation of class II hybrids *via* the sol–gel method. We investigate the effect of the ratio of CL/silane containing units on the mechanical properties of the hybrids and the utilization of the materials that exhibited the desired mechanical properties as "ink" for the preparation of biodegradable 3D-printed, hybrid scaffolds *via* direct-ink writing. We explore the advantages of these hybrid scaffolds, including their gradual degradation and mechanical properties.

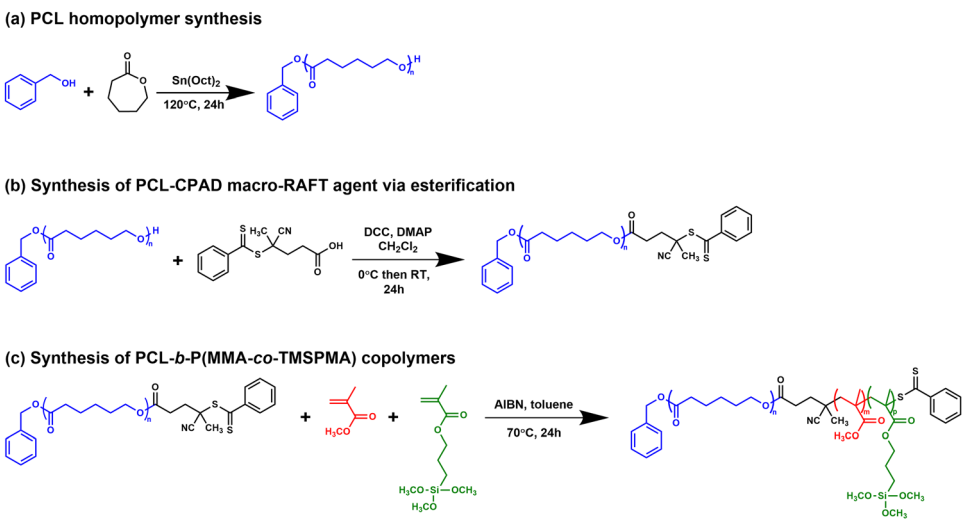
Materials and methods

Materials

ε-Caprolactone (ε-CL, 97%), methyl methacrylate (MMA, 99%), 3-(trimethoxysilyl)-propyl methacrylate (TMSPMA), 4-cyano-4-(phenylcarbonothioylthio)pentanoic acid (CPAD), 2,2′-azobis-(2-methylpropionitrile) (AIBN, 98%), 2,2-diphenyl-1-picryl-hydrazyl hydrate (DPPH, 99%), calcium hydride (CaH_2, 95%), benzyl alcohol (BnOH, 99.8%), tin(II) 2-ethylhexanoate ($Sn(Oct_2)$, 97%) *N*,*N*′-dicyclohexylcarbodiimide (DCC, 99%) 4-(dimethyl-amino)pyridine, (DMAP, ≥99), dichloromethane (DCM, anhydrous ≥99,8%), basic alumina (Al_2O_3, 95%), methanol (≥99,6%), *n*-hexane (95%), toluene (anhydrous, 99,8%), tetrahydrofuran (THF, ≥99.9%), deuterated chloroform ($CDCl_3$, 99.8%), tetraethyl orthosilcate (TEOS, 98%), and hydrochloric acid solution (1 M HCl) were purchased from Sigma-Aldrich UK. The monomers, MMA and TMSPMA were purified by passing through alumina column (basic for MMA and neutral for TMSPMA), to remove inhibitors and acidic impurities, and were stirred over CaH_2 for 1 h to neutralize traces of moisture in the presence of DPPH, while CL was purified by stirring over CaH_2 for 12 h. Finally, all the monomers were vacuum distilled prior to the polymerization. AIBN was recrystallized twice in methanol before use.

PCL synthesis

The synthesis of the PCL homopolymer was accomplished by a typical ROP procedure (Scheme 1(a)). Freshly distilled ε-CL (30 g, 263 mmol), BnOH (2.85 g, 26.3 mmol) and $Sn(Oct)_2$ (1.07 g, 2.63 mmol) were added in a round bottom flask which was degassed under vacuum and filled with Ar prior to use. The mixed solution was further purged with Ar gas bubbling for



Scheme 1 Synthetic route for (a) PCL homopolymer, (b) PCL-CPAD macro-RAFT agent and (c) PCL-*b*-P(MMA-*co*-TMSPMA) copolymers.

 This journal is © The Royal Society of Chemistry 2025

Open Access Article. Published on 27 August 2025. Downloaded on 10/3/2025 4:51:24 PM. This article is licensed under a Creative Commons Attribution 3.0 Unported Licence.

30 min and place in a thermostated oil bath at 120 °C for 24 h. After the termination of the polymerization reaction by the addition of a small amount of methanol, the polymerization mixture was diluted in THF, and the product was isolated by precipitation in large excess of cold methanol. The resultant PCL-OH homopolymer was dried in vacuum oven at room temperature for 72 h (yield 94%) before being used for the preparation of the PCL based RAFT agent.

Synthesis of PCL-CPAD RAFT agent

The PCL-OH homopolymer was converted into a macro-RAFT agent *via* esterification (Scheme 1(b)). In a round bottom flask, PCL (5 g, 1.47 mmol), CPAD (0.82 g, 2.94 mmol) and DMAP (0.09 g, 0.74 mmol) were dissolved in in 45 mL CH_2Cl_2. The solution was cooled to 0 °C and DCC (0.6 g, 2.94 mmol) dissolved in 5 mL CH_2Cl_2 was added to it dropwise. The final mixture was left under stirring at room temperature overnight. The final solution was filtered for the removal of dicyclohexylurea and the filtrate was precipitated in large 10-fold excess of cold methanol. The precipitate was collected and dried in vacuum oven for 72 h.

Synthesis of PCL-*b*-P(MMA-*co*-TMSPMA) copolymers

The PCL based macro-RAFT agent was used for the synthesis of the second P(MMA-*co*-TMSPMA) random block (Scheme 1(c)). Polymers with different MM and compositions were prepared (Table 1-the copolymers are named according to their PCL content). A typical synthesis, aiming for 10 wt% PCL in the final copolymer, is described below. A Schlenk tube was loaded with PCL-CPAD (1 g, 0.25 mmol), freshly distilled MMA (8 g, 80 mmol), TMSPMA (1 g, 4 mmol) and AIBN (0.0205 g, 0.125 mmol) as the radical initiator, and 40 mL toluene as the polymerization solvent. The Schlenk tube was degassed by 3 freeze-vacuum-thaw cycles under Ar and placed in a thermostated oil bath at 70 °C for 24 h. The polymerization reaction was terminated by cooling at −20 °C and exposure to air, and the product was isolated by precipitation in large excess of *n*-hexane. The PCL-*b*-P(MMA-*co*-TMSPMA) copolymer was redissolved in THF and stored in the freezer, to avoid cross-linking of the trimethoxysilyl groups of TMSPMA.

Preparation of PCL-*b*-P(MMA-*co*-TMSPMA)/silica hybrids

Hybrid monoliths were prepared *via* sol–gel in three different inorganic (TEOS)–organic (copolymer) weight ratios (10 : 90, 20 : 80, 30 : 70). TEOS was used as the inorganic silica precursor and was hydrolyzed in distilled H_2O with 1 M HCl for 1 h under stirring. In a second beaker, the appropriate amount of PCL-*b*-P(MMA-*co*-TMSPMA) was dissolved in THF (1 g mL^{-1}). The copolymer solution was added dropwise to the hydrolyzed TEOS and the mixture was stirred for about 10 min. Later, the mixture was cast in polytetrafluoroethylene (PTFE) containers, sealed, and placed in the oven at 40 °C for 25 days for ageing. The container was sealed for the first ten days, and the lid was gradually opened upon complete drying, thereafter. A similar procedure was followed for the preparation of the hybrid ink which was used for 3D printing. In this case, the hybrid mixture was placed in syringes and used when the desired viscosity level for printing was reached.

Gel permeation chromatography (GPC)

The molecular weight and molecular weight distributions of the synthesized polymers were determined by GPC measurements, using an Agilent, SECcurity GPC system, with a polymer standard service (PSS) SDV analytical linear M column (SDA083005LIM). THF containing 5 vol% triethylamine was used as the mobile phase and was pumped with a flow rate of 1.0 mL min^{-1} using a "1260 ISO" isocratic pump. An Agilent 1260 RI detector was used to measure the refractive index (RI) signal. The setup was calibrated with a series of six narrow MM linear PMMA standards (MM ranging from 2–100 kg mol^{-1}). The samples were readily soluble in the mobile phase. Concentrations in the range of 10 mg mL^{-1} were used for analysis.

Nuclear magnetic resonance (NMR)

^1H NMR spectra were recorded on $CDCl_3$ a Bruker AV-400 spectrometer operating at 400 MHz, using tetramethylsilane (TMS) as internal standard and deuterated chloroform ($CDCl_3$) as the solvent. The pulse repetition time was 8.37 s.

Fourier transform infrared spectroscopy (FT-IR)

FT-IR spectra in the region 550–4000 cm^{-1} were obtained on a Thermo Scientific Nicolet iS10 spectrometer equipped with an attenuated reflection (ATR) module.

Uniaxial compression

Uniaxial compression and cyclic loading tests were performed on cylindrical samples (height: 14.70 ± 0.81 mm and diameter: 9.40 ± 0.32 mm) and 3D printed scaffolds, using a Zwick/Roell Z010 instrument equipped with Zwick/Roell "testXpert II" (V3.0) software, fitted with a 10 kN load cell, set in displacement control at a rate of 1 mm min^{-1}. The top and bottom of the samples were manually ground to flat with SiC paper before measurement.

Table 1 Molecular characteristics of PCL-*b*-P(MMA-*co*-TMSPMA) copolymers. $Đ^a$ is the molar mass dispersity

Sample	Abbreviation	$M_n{}^a$ (g mol^{-1})	$Đ^a$	% wt PCL[b]	% wt PMMA[b]	% wt TMSPMA[b]
PCL-CPAD	—	3500	1.12	100	—	—
PCL-*b*-P(MMA-*co*-TMSMPA)-1	PCL37	8100	1.65	37	55	8
PCL-*b*-P(MMA-*co*-TMSMPA)-2	PCL29	14 000	1.60	29	65	6
PCL-*b*-P(MMA-*co*-TMSMPA)-3	PCL16	30 400	1.52	16	74	10

[a] Determined by GPC. [b] Calculated by ^1H-NMR in $CDCl_3$.

Open Access Article. Published on 27 August 2025. Downloaded on 10/3/2025 4:51:24 PM. This article is licensed under a Creative Commons Attribution 3.0 Unported Licence.

Dissolution studies

Phosphate-buffered saline solution (PBS) was chosen for studies in wet environment. PBS was prepared by dissolving a 5 g solid tablet (Gibco®, Thermo Fisher Scientific, Hemel Hempstead, UK; composition: 10 mM sodium phosphates, 140 mM NaCl, 2.68 mM KCl) in 500 mL of deionized water and the final pH was verified to be 7.45. The aim of the study was to evaluate the effect of an aqueous solution at neutral pH (7.45) and body temperature (37 °C) on the properties of the hybrids up to 3 months. Since PCL and silica are slowly biodegradable, whereas methacrylate part of the polymer chain is not, only a slight degradation was expected. After soaking monolithic samples in PBS (1.5 mg of hybrid per 1 mL of PBS) for 3 months, first a macroscopic observation, in terms of possible swelling, creation of defects, visible degradation of the monolithic samples, was done, from which specific compositions were selected for further study. Acidic system also used to study the degradation of hybrid. 2 M HNO_3 (nitric acid N.A.) is used as medium. Sample solutions were diluted to a factor of 10 using analytical grade 2 M HNO_3. Silicon standards were applied in this study at 0, 10, 50 μg mL^{-1} (parts per million) concentrations for calibration. Concentration of Si in solution was measured with Thermo Scientific iCAP6300 Duo inductively coupled plasma–optical emission spectrometer (ICP-OES) with auto sampler. Standards of Si (#1.70365.0100, Merck) were prepared at 0, 1, 2, 5, 10, 20 and 40 μg mL^{-1} and used as calibration curve. Calibration was carried out at the beginning of each sequence. Si was measured in the radial direction. Each treatment was tested in triplicate and each sample was measured three times in ICP. ICP results were averaged over three repeat measurements of three replicates of each treatment. Results are shown as mean ± standard deviation.

X-Ray micro-computed tomography (micro-CT)

The 3D printed samples produced with hybrid ink material were imaged using a laboratory-based μCT system (ZEISS Xradia 510 Versa). The X-ray source was operated at 50 kV and exposure time of 3 s. Captured projections were reconstructed using filtered back projection algorithm resulting in a 3D image matrix of 250 × 256 × 252 with isotropic voxel size of 20.67 μm. Each sample was scanned three times. 3D ImageJ suite plugin of ImageJ software was used for the determination of the strut size and channel size distributions.

To calculate the porosity percentage and channels interconnectivity, a sub-volume of interest (2000 × 2000 × 2000 μm) was defined for quantification. Manual thresholding was performed by selecting the mid-point between attenuation peaks was selected using Avizo software (2023 version). ''Label analysis'' in Avizo was utilized for the measurement of porosity and interconnectivity (percentage of pores connected with each other and the exterior).[41] Channel size of T29 scaffolds were measured using the BoneJ plugin at ImageJ software.

Scanning electron microscopy (SEM)

SEM measurements were conducted on a JEOL 6010LA instrument, with an accelerating voltage of 20 kV; a working distance of 12 mm; and a spot size of 60 mm. Prior to imaging, samples were made conductive by coating with a layer of gold. The top surface and cross section of the samples were investigated. ImageJ software was utilized for the analysis of the obtained micrographs.

Thermogravimetric analysis (TGA)

TGA measurements were conducted on a NETZSCH STA 449C TGA instrument. Samples were ground to fine powder and placed in a platinum crucible. The samples were then heated to 800 °C at 10 °C min^{-1} with continuously supplied air to burn away organic components.

3D printing

The sol–gel ink was prepared following the procedure described above for the preparation of PCL-*b*-P(MMA-*co*-TMSPMA)/glass hybrids and submerged in a syringe. Residual air was manually removed, and the syringe was placed in a robocasting machine (''Robocaster'', 3d Inks LLC, USA). The scaffold architectures (CAD files) were designed using 'Robocad' software, which was also used to control the printing process of the porous scaffolds according to the drawn design. The gelation process continued in the syringe, leading to a progressive increase in viscosity. The porous scaffolds where then 3D printed when the viscous sol reached the optimal viscosity for direct extrusion (decided by tilting the syringe and observing the viscosity–gelation time varied according to organic–inorganic ratio used) using PTFE as substrate. A smooth-flow tapered tip with a nozzle of 0.20 mm internal diameter was used at a printing speed of 10 mm s^{-1}. Each layer consists of a linear array of parallel rods and alternating layers oriented at 90° to each other. The strut separation (defined as the spacing between the axis of the adjacent parallel rods) was set from 0.8 mm to 1.0 mm. Each layer was plotted applying a constant deposition rate of 0.05 mL min^{-1} and using a layer thickness (*i.e. z*-spacing) of 0.21 mm.

As-prepared 3D printed cubical scaffolds consisted of a wet gel and were placed in Nalgene PMP containers with screwed lid at 40 °C for ageing over the course of 3 days. Ageing continued for 4–7 days (upon complete drying) by gradually unscrewing the lid. Any impurities were then removed by immersion in deionized H_2O for 30 seconds. Following the shrinkage cause by drying, the side dimensions of the dry scaffolds range between 9.6–12.0 mm.

Biological characterization

Cell subculture and sample preparation. Fresh unprocessed human bone marrow stromal cells (h-BMSCs, #PT2501, LONZA) were routinely subcultured using the POEITICS™ MSC SingleQuots® kit at 37 °C and 5% CO_2 (using 0.05% trypsin–EDTA, Thermo Fisher Scientific). The cells were expanded near confluency (~90%) in alpha-MEM + glutamax (#32561, Gibco) containing 10% (v/v) heat inactivated foetal bovine serum (FBS, Life Technologies), 1% (v/v) penicillin–streptomycin (Pen-Strep, Invitrogen) and 0.1% amphotericin B (A2942, Sigma). Cells were used up to passage 5 at population doubling level 5.61. Human-BMSCs were seeded 1 × 10^4 cells per well in

 This journal is © The Royal Society of Chemistry 2025

Open Access Article. Published on 27 August 2025. Downloaded on 10/3/2025 4:51:24 PM. This article is licensed under a Creative Commons Attribution 3.0 Unported Licence.

the central portion (columns 2–11, rows B–G) of 96 microwell plates with black-walled and clear bottom (#3340, Corning). The peripheral wells were left acellular and filled in with medium only.

Conditioned medium preparation. Sterile PCL29 (organic/inorganic: 70–30, 80–20 and 90–10) hybrid discs were immersed in a predefined volume of serum-free DMEM (#11880, Gibco) in accordance to ISO10993-12 (sample preparation and reference materials – 0.65 cm^2 $hybrid^{-1}$ disc, 4.6 discs per mL of fresh serum-free DMEM to give 3 cm^2 mL^{-1}). After a 72 h incubation at 37 °C, the extracts were directly sterilized by filtration through a 0.2 μm non-pyrogenic sterile 28 mm syringe surfactant-free cellulose acetate filter (#431219, Corning). Dilution series of 25%, 50%, 75% and 100% were prepared from the extracts with DMEM (called vehicle, VC) incubated in identical conditions. The conditioned media were directly used for the *in vitro* cytotoxicity assay.

***In vitro* cytotoxicity assay.** Cytotoxicity effects of PCL29/70-30, PCL29/80-20 and PCL29/90-10 hybrid discs on h-BMSCs was assessed in accordance to ISO 10993-5 (tests for *in vitro* cytotoxicity) and ISO 10993-12 standards. Conditioned media were prepared as detailed above. High density polyethylene (PE) film (negative reference material, RM-C cut, thickness 0.5 mm, 2 × 15 mm, 0.3 cm^2 from Hatano Research Institute, Food and Drug Safety Center, Japan) was used as negative control (non-cytotoxic) and polyurethane (PU) containing 0.1% (w/w) zinc diethyldithiocarbamate (ZDEC) (RM-C cut, thickness 0.5 mm, 2 × 15 mm, 0.3 cm^2) was used as positive control (reproducible cytotoxic from Hatano Research Institute, Food and Drug Safety Center Japan). For all conditioned media, sterilization was achieved by filtration through a 0.2 μm non-pyrogenic sterile 28 mm syringe surfactant-free cellulose acetate filter. Prior to treating cells, all conditioned media were supplemented with 10% (v/v) FBS, 1% (v/v) P/S, 0.1% Amphotericin B and 1% (v/v) L-glutamine. The cells were treated with 100 μL per well (n = 6 wells per condition). After 24 hours of treatment, colorimetric metabolic activity assay was carried out to assess cell viability based on the conversion of 3-(4,5-dimethylthiazol-2-yl)-2,5-diphenyltetrazolium bromide (MTT, M5655, Sigma) into (purple) formazan crystals. The assay was performed 96 microwell plates with black-walled and clear bottom (#3340, Corning). Briefly, the used media was replaced with solution of MTT in serum-free DMEM at a concentration of 1 mg ml^{-1} (50 μl $well^{-1}$). After 2 hours of incubation, the solution was removed and 100 μL of isopropanol was added to dissolve the formazan crystals. Following 15 min gentle shaking at room temperature, the absorbance at 570 ± 15 nm was measured on a SpectraMax I3x reader with SoftMax Pro 7 software (Tecan, Molecular Devices, UK).

Total DNA content. Total DNA content was quantified using Quant-iT™ PicoGreen™ dsDNA Assay Kit (PT11496, Invitrogen). Briefly, each well was carefully washed once in PBS and then submerged in 115 μL of TE lysis buffer containing 10 mM Tris (pH 8), 1 mM EDTA, 0.2% (v/v) Triton X-100 and 0.1 mg mL^{-1} proteinase K. The wells were sealed and incubated overnight at 4 °C on an orbital shaker to release the DNA. Thereafter, each sample was homogenized by vigorous pipetting. Cell lysates were incubated with Quanti-IT PicoGreen dye at room temperature in a 96 microwell plate with black-walled and clear bottom (#3340, Corning) for 5 min, protected from light. Then, the fluorescence intensity was measured at an excitation wavelength of 480 ± 9 nm and an emission wavelength of 520 ± 15 nm.

Statistical analyses. All results are reported as mean ± standard deviation of at least three independent experiments ($N \geq 3$), unless otherwise stated. The samples were prepared at least in sextuplet ($n \geq 6$) (for each condition and for each independent experiment). Statistical analyses were carried out using a non-parametric Kruskal–Wallis multiple comparisons test. Statistical analyses were carried out using GraphPad Prism (version 9.1.1 for MacOS, GraphPad Software, San Diego, California USA, **https://www.graphpad.com**). p values are indicated in figure captions.

Results and discussion

Copolymer synthesis

The synthesis of the PCL-*b*-P(MMA-*co*-TMSPMA) copolymers with various compositions was accomplished in three steps (Scheme 1). Initially, the PCL homopolymer was synthesized *via* ROP (Scheme 1(a)).

The PCL homopolymer was then reacted with CPAD to form the PCL-CPAD macro-RAFT agent *via* esterification (Scheme 1(b)). A mean degree of esterification of 86% for this precursor was calculated by ^{1}H-NMR, by comparing the integrated proton signal at 1.91 ppm assigned to the methyl group of the RAFT agent with the PCL backbone signals at 4.07, 2.33 and 1.66 ppm (Fig. S1).

Finally, PCL-CPAD was used for the preparation of the P(MMA-*co*-TMSPMA) block (Scheme 1(c)). The molecular characteristics of all PCL-*b*-P(MMA-*co*-TMSPMA) copolymers are presented in Table 1.

The synthetic procedure resulted in copolymers with monomodal molecular weight distributions with the molar mass dispersity ranging between 1.50–1.65 and good control over the molar mass and compositions (Table 1). The results are similar to previous publications where ROP and RAFT were combined.[42,43] The chromatograms shown in Fig. 1 indicate the successful synthesis of three copolymers with different molar masses. It should be noted that the dispersity index decreased as the molar mass of the polymer increases as expected for a control/living polymerization method, indicating successful polymerization. The moderately broad molecular weight distributions arise from the challenges of RAFT polymerization for methacrylates, particularly when using a PCL-based macro-RAFT agent. Inherent termination rates of methacrylates and potential side reactions with TMSPMA's silane groups contribute to this outcome. However, the monomodal SEC traces and successful block copolymer formation, as evidenced by ^{1}H-NMR spectroscopy and TGA measurements, confirm architectural control sufficient for the intended purpose of the hybrids.

Open Access Article. Published on 27 August 2025. Downloaded on 10/3/2025 4:51:24 PM.
This article is licensed under a Creative Commons Attribution 3.0 Unported Licence.

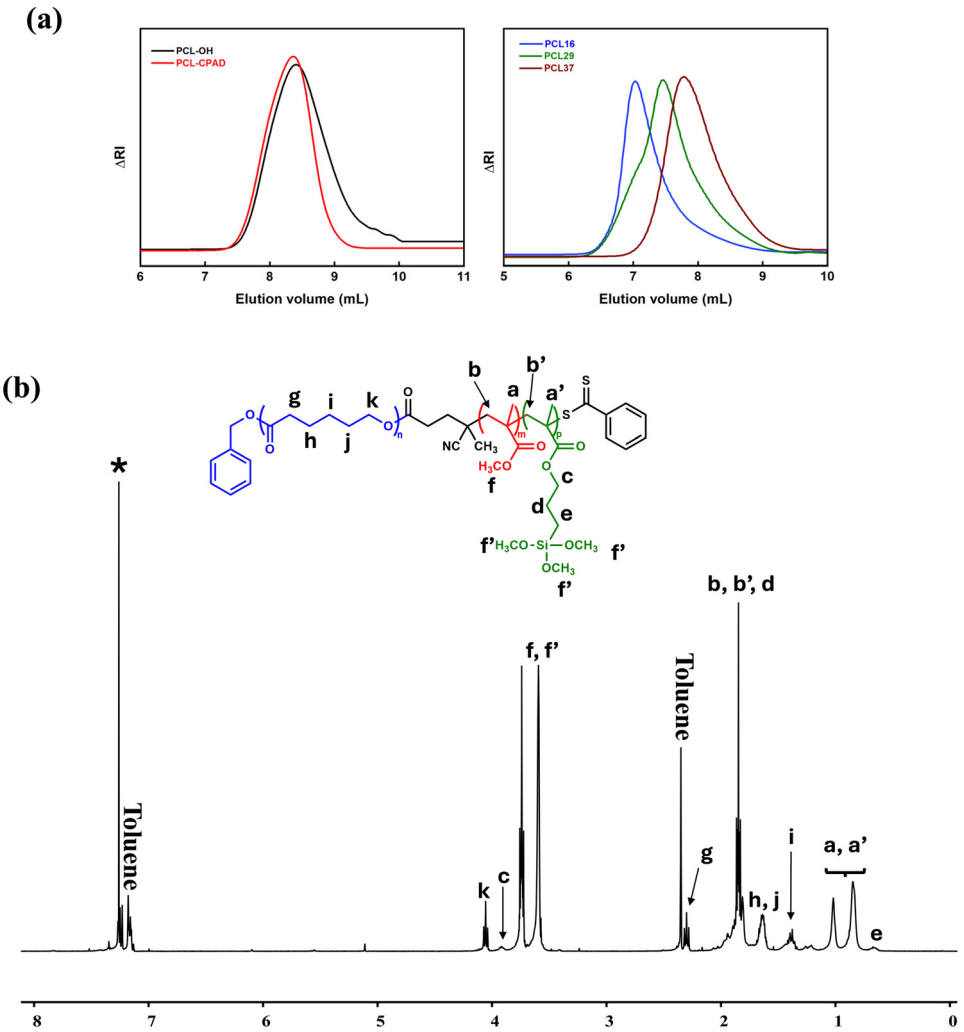


Fig. 1 (a) SEC chromatograms of PCL-OH and PCL-CPAD precursors (left) and of all PCL-*b*-P(MMA-*co*-TMSPMA) copolymers synthesized (right). Sample codes are explained in Table 1; (b) ^{1}H-NMR spectrum of PCL-*b*-P(MMA-*co*-TMSMPA)-2, PCL29, in $CDCl_3$.

The chemical structure and composition of the PCL-*b*-P(MMA-*co*-TMSPMA) copolymers were confirmed by ^{1}H-NMR measurements (Fig. 1(b)). The compositions of the terpolymers were found to be in close proximity to the theoretical calculations, based on the stoichiometry and polymerization yield after each step (Table 1). The spectral peaks used for the calculations are at 2.29 ppm (–CH_2–CH_2–CH_2– of PCL), at 3.6 ppm (–OCH_3 of MMA and –Si–$(OCH_3)_3$ of TMSPMA) and 0.67 ppm (–CH_2–Si– of TMSPMA). The chemical shifts associated with CPAD are not visible in the acquired spectra, because concentration is very low in comparison with the chemical shifts that correspond to the copolymer.

PCL-*b*-P(MMA-*co*-TMSPMA)/silica hybrid monoliths

The PCL-*b*-P(MMA-*co*-TMSPMA) copolymers were then utilized for the fabrication of cylindrical shaped, class II PCL-*b*-P(MMA-*co*-TMSPMA)/silica hybrids with three different inorganic/organic weight ratios *via* sol–gel (Fig. 2(a)). Crack-free hybrids were obtained (Fig. 2(b)), with their color attributed to the RAFT agent. The color was yellow when the PCL, and subsequently the CTA, amount was the lowest. The color turned orange when higher PCL ratios were utilized (more CTA present).

FT-IR spectra (Fig. 2(c)) contained characteristic vibration bands for both the copolymers and silica network in the hybrid system. Vibration bands expected in methacrylate-based polymers were present in all three copolymer spectra: C–H vibration (2950, 1485 cm^{-1}, methacrylate backbone); C═O (1725 cm^{-1}); C–C–O (1239 cm^{-1}, asymmetric stretching), and C–O–C, symmetric stretching (1140 cm^{-1}) of the ester group from the methacrylate moieties. Characteristic peaks corresponding to the condensed silica network can be observed at 1130 and 790 cm^{-1} (Si–O–Si, asymmetric stretching), and 950 cm^{-1} (Si–OH, hydrogen bonded, stretching). The band at 560 cm^{-1} is assigned to Si–O bending vibrations, indicative of the silicate network structure. The appearance of this band, alongside the Si–O–Si stretching at 780 cm^{-1}, confirms the successful condensation and network formation of the inorganic phase.

 This journal is © The Royal Society of Chemistry 2025

Open Access Article. Published on 27 August 2025. Downloaded on 10/3/2025 4:51:24 PM.
This article is licensed under a Creative Commons Attribution 3.0 Unported Licence.

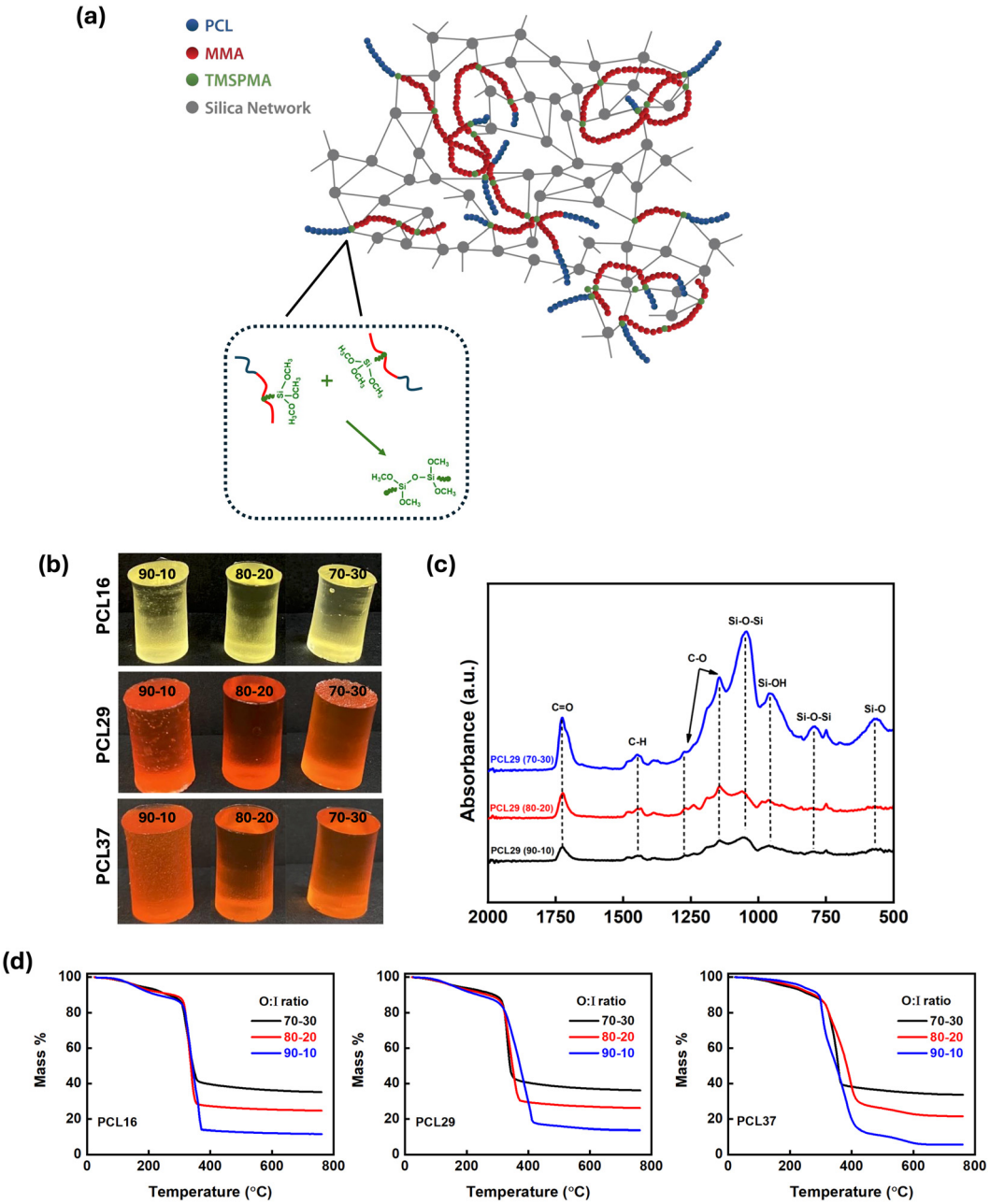


Fig. 2 (a) Schematic illustration of the formation of PCL-*b*-P(MMA-*co*-TMSPMA)/silica hybrids; (b) photographs of hybrid monoliths prepared using each the PCL-*b*-P(MMA-*co*-TMSPMA) copolymers (Table 1) and organic/inorganic (O : I) ratios 90 : 10, 80 : 20 and 70 : 30; (c) FTIR spectra of the hybrids prepared with PCL29 copolymer; (d) TGA thermograms of hybrids monoliths for all 3 PCL-*b*-P(MMA-*co*-TMSPMA) copolymers.

TGA analysis measurements, performed to determine the final inorganic/organic ratio of the hybrids (Fig. 2(d)), revealed thermal decomposition of the organic components initiating at *ca.* 300 °C. The inorganic component ratio was close to the theoretically targeted compositions.

Compression curves of cylinder-shaped hybrids (Fig. 3(a)) exhibited clear elastic and plastic deformation regimes, except hybrids made with PCL16 (inorganic/organic: 30/70) that only showed elastic deformation. This is because in the PCL16 (inorganic/organic: 30/70) hybrid, the copolymer with the highest molar mass was used and the inorganic/organic ratio was *ca.* 35/65, making the hybrid more stiff. As the molar mass of the copolymer and the inorganic ratio increased, the yield stress increased. The highest yield stress values were recorded for samples comprising inorganic/organic ratio of 70 : 30. The results indicate that the PCL content affects the mechanical properties of the copolymer/silica hybrids. Specimens prepared with the copolymer bearing the lowest PCL : TMSPMA ratio (PCL16) were more brittle but demonstrated the highest yield stress in all inorganic : organic ratios investigated. Specimens prepared with PCL29 and inorganic : organic ratio of 70 : 30 are the only exception, recording the highest yield stress

Open Access Article. Published on 27 August 2025. Downloaded on 10/3/2025 4:51:24 PM.
This article is licensed under a Creative Commons Attribution 3.0 Unported Licence.

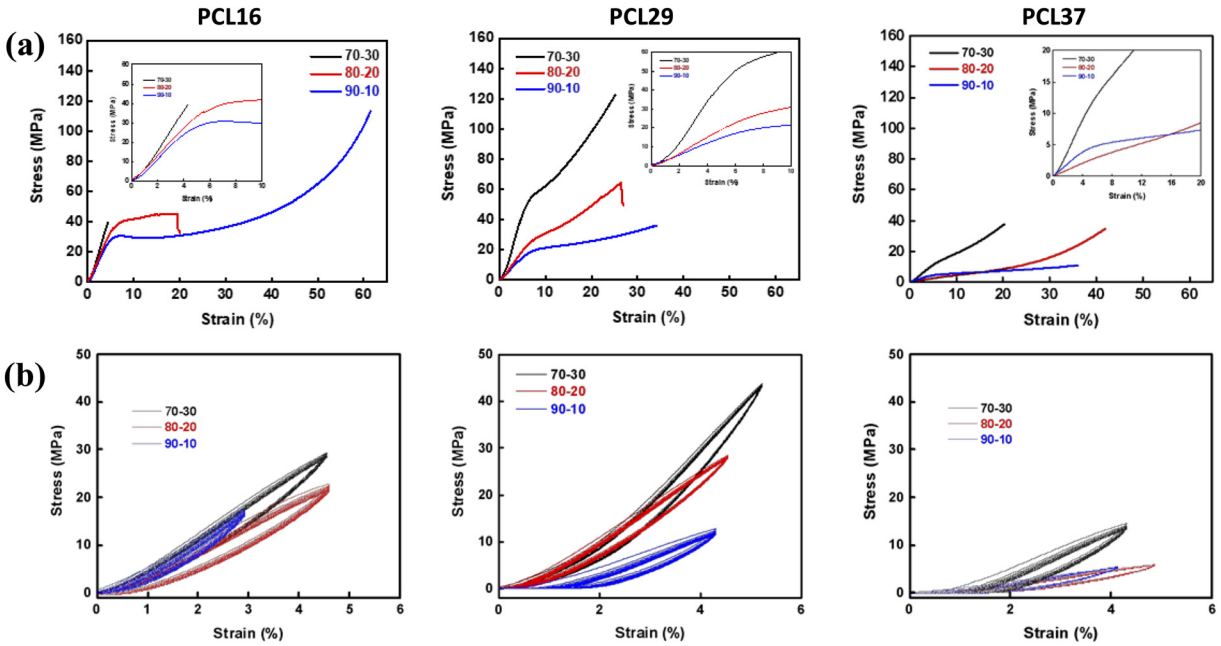


Fig. 3 Uniaxial compression (a) and cyclic compression (b) test curves for PCL-*b*-P(MMA-*co*-TMSPMA)/silica hybrid monoliths at different organic/inorganic ratios.

Table 2 Compression testing results for PCL-*b*-P(MMA-*co*-TMSPMA)/silica hybrids

Sample	Theoretical org.–inorg. (%)	Org.–inorg.[a] (%)	Yield stress[b] (MPa)	Yield strain[b] (%)	Stress at failure[b] (MPa)	Strain at failure[b] (%)
PCL16	70–30	64.8–35.2	39.3 ± 4.0	4.3 ± 0.5	39.3 ± 4.0	4.3 ± 0.5
	80–20	75.2–24.8	35.9 ± 2.0	5.7 ± 0.4	44.9 ± 2.0	19.5 ± 0.6
	90–10	88.4–11.6	28.0 ± 1.0	5.8 ± 0.4	113.4 ± 7.0	61.5 ± 4.0
PCL29	70–30	64.6–35.4	52.9 ± 5.0	6.3 ± 0.5	122.6 ± 8.0	25.2 ± 1.6
	80–20	74.2–25.8	24.5 ± 1.4	6.7 ± 0.5	64.5 ± 4.0	26.4 ± 2.2
	90–10	86.5–13.5	17.8 ± 1.2	6.8 ± 0.6	34.0 ± 3.0	36.0 ± 2.4
PCL37	70–30	66.3–33.7	13.8 ± 1.0	6.5 ± 0.5	37.7 ± 4.0	20.3 ± 1.8
	80–20	78.5–21.5	9.1 ± 1.0	19.9 ± 1.0	34.7 ± 2.8	41.9 ± 2.5
	90–10	94.2–5.8	4.8 ± 0.4	5.8 ± 0.5	10.9 ± 1.6	36.0 ± 3.0

[a] Calculated by TGA. [b] Measured by uniaxial compression.

(52.9 ± 2.0 MPa). Overall, the yield stress values appear to be higher when PCL : TMSPMA ratio is lower. All uniaxial compression data are summarized in Table 2.

Our group has previously reported the synthesis of linear P(MMA-*co*-TMSPMA), P(BMA-*co*-TMSPMA) and P(MA-*co*-TMSPMA) copolymers by RAFT polymerization, and their utilization for the preparation of hybrids.[44] The yield stress values recorded for those hybrids (inorganic : organic 30 : 70) were 25 ± 0.3 MPa, 17 ± 3.0 MPa and 18 ± 3.0 MPa respectively. The incorporation of PCL does not seem to reduce the mechanical properties as the yield stress values recorded for PCL-*b*-P(MMA-*co*-TMSPMA)/silica hybrids (inorganic : organic 30 : 70 and 80 : 20) are significantly higher for samples prepared with PCL16 and PCL29. The yield strain is comparable for copolymers with and without PCL. The molecular weight of the copolymers is another parameter that must be taken into account, as PCL16 has significantly higher molar mass than the P(MMA-*co*-TMSPMA), P(BMA-*co*-TMSPMA) and P(MA-*co*-TMSPMA) copolymers.

Previously, we have also reported polymer/silica hybrids (organic : inorganic ratio 70 : 30) prepared with star-shaped macromolecular architectures comprising P(MMA-*co*-TMSPMA) arms and EGDMA cores and randomly branched P(MMA-*co*-TMSPMA) copolymers.[45] Hybrids made with star copolymers had a yield stress of 26 ± 3.0 MPa and yield strain of 4.8 ± 1.0% and the branched copolymers have a yield stress of 51 ± 8.0 MPa and yield strain of 6.1 ± 1.5%. Again, it seems that at similar organic : inorganic ratios, linear PCL-*b*-P(MMA-*co*-TMSPMA) copolymers can produce hybrids with comparable yield stress values and somewhat lower yield strain percentages. This is a very important observation, since a biodegradable block has now been incorporated in the copolymer architecture.

The ability of the hybrids to take cyclic loads was also investigated in order to evaluate their suitability for bone regeneration under physiological loads. Such tests address the clinical need for materials that avoid stress shielding while enduring repetitive physiological stresses, as highlighted in studies on bioactive

 This journal is © The Royal Society of Chemistry 2025

Open Access Article. Published on 27 August 2025. Downloaded on 10/3/2025 4:51:24 PM.
This article is licensed under a Creative Commons Attribution 3.0 Unported Licence.

glasses and ceramic/polymer composites. Each sample was subjected to 11 cycles, reaching at 60% of strain relative to the linear elastic region strain values. The obtained results revealed 11 cycles of approx. overlapping stress–strain profiles (Fig. 3(b)). This proves that all samples and were able to recover the deformation and retain their original shape at the given strain (minor energy loss between cycles), when the load was removed. Cyclic loading stability over 11 cycles demonstrates fatigue resistance critical for load-sharing applications.

The different mechanical properties obtained at the same organic/inorganic ratio, *e.g.* 80–20 (Table 2) for hybrids made with polymers with different TMSPMA content (PCL16, PCL29 and PCL37), indicate successful covalent coupling between the inorganic and organic networks. If the results were similar, they would indicate that covalent coupling had not occurred.

PCL-*b*-P(MMA-*co*-TMSPMA)/silica 3D-printed hybrid scaffolds

The hybrid ratios that exhibited the mechanical properties with the highest combination of yield stress and strain values were those made with PCL16 and PCL29 at organic/inorganic ratio of 70/30. These compositions were utilized as hybrid ink for the preparation of 3D-printed scaffolds. This was achieved *via* 3D extrusion printing directly from the sol–gel, to benefit from the fact that viscosity would increase with time and eventually reach gelation. Inks with 70 : 30 organic : inorganic ratios were prepared with PCL16 and PCL29 as the ink printing window (optimum viscosity) was approximately 1 h.

The resulting 3D printed hybrid scaffolds are shown in Fig. 4(a) and (b). The morphology of the 3D printed scaffolds was imaged by SEM. Micrographs of the top surface, horizontal and vertical sections were acquired (Fig. 4(c)–(e)). The strut size used ranged from 0.8–1.0 mm for all scaffolds. The images show an overall regularity in reproducing the designed pattern and there is no evidence of collapsing of the struts. Pore channels were visible on both horizontal and vertical sections, demonstrating complete interconnection in all directions. The average pore size (diameter of interconnected channels between printed struts, measured post-drying using) of the scaffolds increases with strut spacing. For scaffolds prepared with PCL16 "ink" the average pore size was 234 ± 25 μm and 362 ± 19 μm for 0.8 and 1.0 mm strut spacing, respectively. The corresponding pore sizes for scaffolds prepared with PCL26 "ink" were 269 ± 20 μm and 380 ± 27 μm, respectively.

Shrinkage does occur in the sol–gel hybrids after printing, during aging and drying, as a result of the continued gelation/polycondensation, undergo shrinkage, reducing pore sizes by ~70% compared to CAD values. For example: 0.8 mm strut spacing (CAD) led to a 234 ± 25 μm pore size in PCL16 scaffolds and 1.0 mm strut spacing (CAD) resulted in a 362 ± 19 μm pore size in PCL16 scaffolds.

Three-dimensional rendering reconstruction of μCT scans revealed that porosity of approximately 48–56% was achieved (Fig. 5). These values are below the porosity of trabecular bone (70–95%).[46] However, the rationale behind the necessity of a porous structure is to provide open pore channels and interconnectivity that are conducive to tissue ingrowth, creating a scaffold for bone to grow on, rather than to recreate a bone structure directly.[47] Due to the channel-like structure, it is challenging to classify the channels into pores and connecting apertures (as done in previous studies,[48–51] but Fig. 5(c) and (f)) show representation of the channels (with the scaffold removed). The mean channel size diameter for PCL29 scaffolds prepared with strut size of 0.8 mm was 263 ± 74 μm, with a maximum of μm (Fig. 5(c)). For PCL29 scaffolds prepared with strut size of 1.0 mm the porosity was 48% and the mean pore equivalent diameter was 320 ± 107 μm, with a maximum of 570 μm (Fig. 5(f)).

The mechanical properties of the 3D printed scaffolds were also evaluated *via* uniaxial compression tests (Fig. 6(a)). The difference in the average pore size as the strut spacing

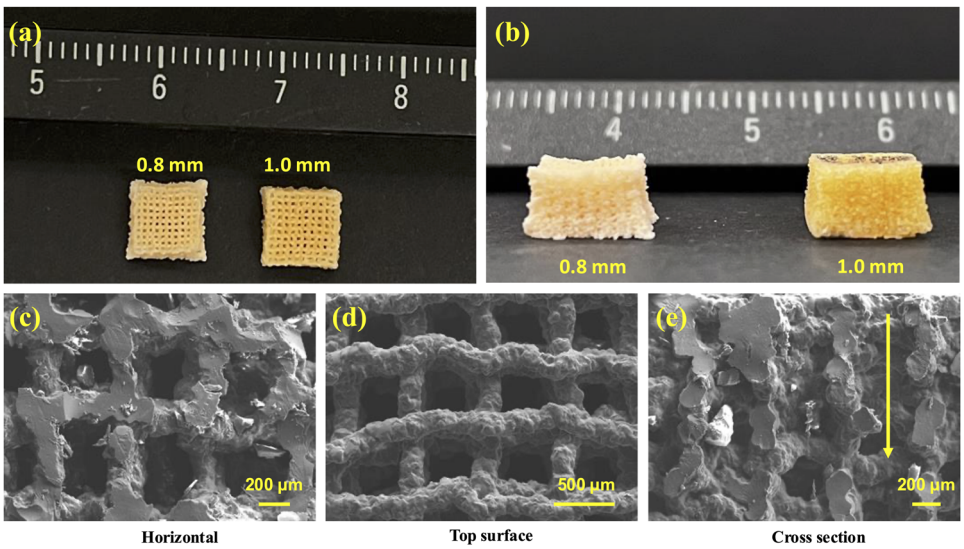


Fig. 4 Top (a) and side (b) side view photos; horizontal section (c), top surface (d) and cross-section (e) SEM micrographs of 3D printed hybrid scaffolds prepared with PCL29 copolymer with inorganic to organic ratio of 30% and strut size of 1.0 μm.

Open Access Article. Published on 27 August 2025. Downloaded on 10/3/2025 4:51:24 PM.
This article is licensed under a Creative Commons Attribution 3.0 Unported Licence.

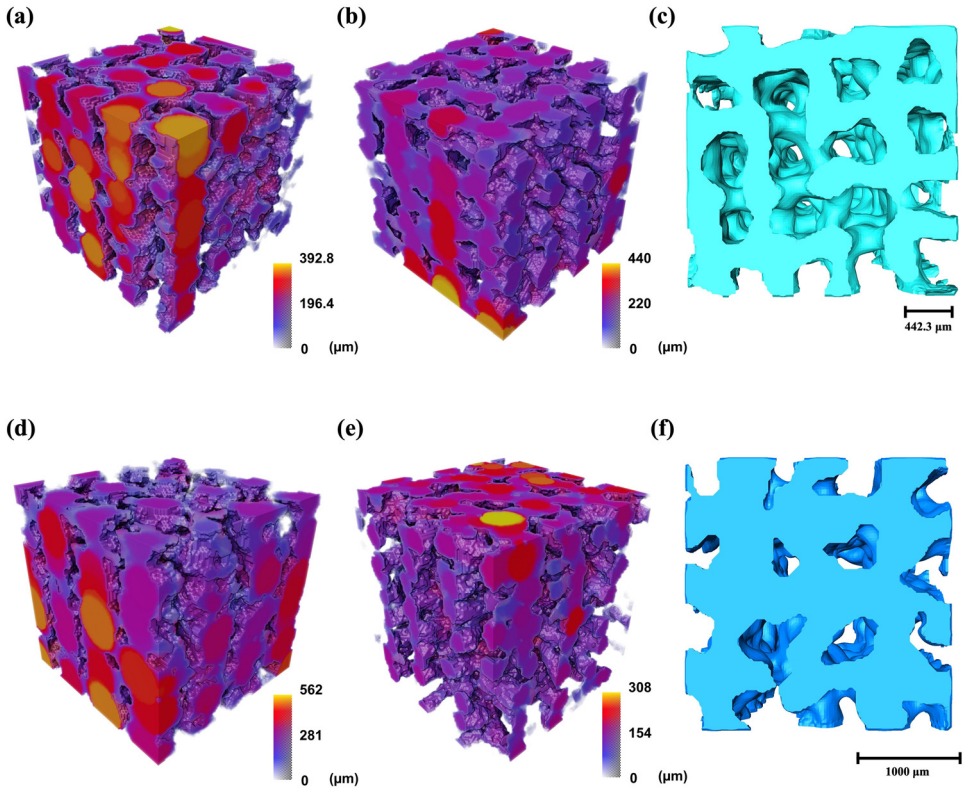


Fig. 5 μCT imaging and analysis of PCL29 3D printed scaffolds. Colour map to visualize the channel size of PCL29 scaffolds prepared with strut size 0.8 mm (a) and 1.0 mm (d); colour map to visualize the interconnecting channel thickness of PCL29 scaffolds prepared with strut size 0.8 mm (b) and 1.0 mm (e); sub-volumes of interest (2000 × 2000 × 2000 μm) of PCL29 scaffolds prepared with strut size 0.8 mm (c) and 1.0 mm (f).

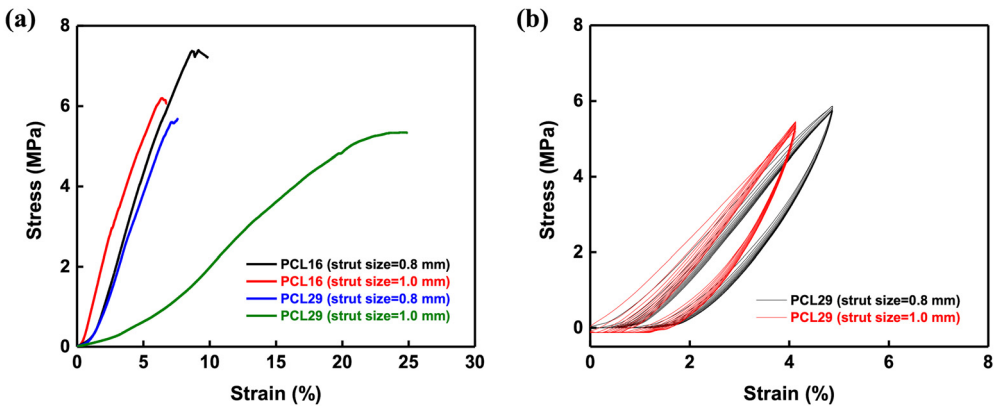


Fig. 6 Representative uniaxial compression test curves for 3D printed hybrid scaffolds of PCL16 and PCL29 (organic/inorganic: 70/30), printed with strut sizes of 0.8 mm and 1.0 mm (left), and cyclic compression test curves of the 3D printed hybrid PCL16 scaffolds (right).

increased supports the mechanical behavior of the scaffolds. A decrease in the values of stress as the pore size increased was observed in all cases. For scaffolds produced with PCL16 copolymer, the stress decreased from 7.5 MPa to 6.4 MPa, while the decrease was less for PCL29 (from 5.6 MPa to 5.2 MPa respectively). This trend is consistent with established structure–property relationships in porous biomaterials, where larger pores reduce the density of load-bearing struts, thereby lowering mechanical strength.[6,7] This inverse correlation is well documented in the literature and reflects the balance between mechanical integrity and biological performance.[52] Smaller pores enhance the mechanical strength of the scaffolds, while larger pores (200–400 μm) are more favorable for nutrient diffusion, angiogenesis, and bone tissue ingrowth. The pore size range achieved in this study (234–380 μm) falls within the optimal window for bone tissue engineering, balancing the need for mechanical support with the requirements for cell migration and vascularization.[52] Thus, these scaffolds hold

 This journal is © The Royal Society of Chemistry 2025

Table 3 Compression testing results for 3D printed scaffolds of PCL16 and PCL29 (organic/inorganic: 70/30)

Sample	Strut size (mm)	Pore size[a] (μm)	Yield stress[b] (MPa)	Yield strain[b] (%)	Stress at failure[b] (MPa)	Strain at failure[b] (%)
PCL16	0.8	234 ± 25	7.4 ± 0.5	8.7 ± 0.5	7.4 ± 0.5	8.7 ± 0.5
	1.0	362 ± 19	6.5 ± 0.2	6.2 ± 0.2	6.5 ± 0.2	6.2 ± 0.2
PCL29	0.8	269 ± 20	5.6 ± 0.3	7.1 ± 0.5	5.6 ± 0.3	7.1 ± 0.5
	1.0	380 ± 27	5.2 ± 0.3	21.4 ± 1.0	5.4 ± 0.4	24.9 ± 1.0

[a] Determined by SEM. [b] Determined by uniaxial compression measurements.

Open Access Article. Published on 27 August 2025. Downloaded on 10/3/2025 4:51:24 PM. This article is licensed under a Creative Commons Attribution 3.0 Unported Licence.

potential for applications in bone regeneration where both structural stability and biological integration are critical. The results are summarized in Table 3.

Cyclic loading measurements (Fig. 6(b)) were also carried out to investigate the capability of the porous 3D printed scaffolds to recover deformation. All scaffolds prepared with both PCL16 and PCL29 exhibited minor differences between the first and the following 10 loading cycles, which fully overlap. Interestingly, all tested scaffolds were able to recover their original shape after the test.

Dissolution studies were performed in PBS to investigate the effect of architecture on the dissolution of the 3D printed scaffolds. According to ICP-OES measurements (Fig. 7(a)), a rapid initial Si release of ~60 μg mL^{-1} was observed during the first 10 days for scaffolds prepared with strut size 1.0 mm. From day 10–120 there was a plateau reached where the Si release remained unchanged. Slow Si release was recorded from day 120–180, reaching a final value of ~70 μg mL^{-1}. Scaffolds printed with a strut size of 0.8 mm, also showed a rapid initial Si release of ~50 μg mL^{-1} over the first 10 days. The lower initial release in this case was attributed to the narrower pore size. Then, Si release increased and reached ~60 μg mL^{-1} after 20 days. From days 20–100 a plateau was also observed, as for scaffolds prepared with strut size 1.0 mm, with the [Si] hovering around 60 μg mL^{-1}. Finally, a slow Si release is observed for day 120–180, reaching a final value of ~70 μg mL^{-1}.

The rapid initial Si release could be due to the release of surface-available silicon or silicon close to the scaffold's surface, as these regions are more exposed to the surrounding medium. The scaffolds with strut size of 1.0 mm showed a slightly higher Si release compared to those with a strut size of 0.8 mm throughout the experiment. This suggests that the wider strut size provides more pathways or surface area for the medium to access the embedded silica, leading to slightly increased release. The 0.8 mm strut scaffolds likely have a denser structure, which may restrict the diffusion of silicon, resulting in marginally lower silicon concentration over time.

The sustained availability of soluble silica species is beneficial, as they are known to stimulate osteogenic activity and support bone regeneration.[53] Therefore, the scaffolds not only provide mechanical support but also deliver bioactive cues that can enhance bone tissue healing.

PCL is a slow-degradable aliphatic polyester, with complete resorption typically taking 2 to 3 years in physiological environments due to its semi-crystalline, hydrophobic structure.[54] This extended degradation period makes PCL ideal for long-term tissue engineering applications such as scaffolds and drug delivery systems.[39] After exposure of PCL-*b*-P(MMA-*co*-TMSPMA)/silica 3D printed scaffolds to PBS, their degradation was investigated by TGA measurements (Fig. 7(b)). For scaffolds prepared with PCL29 and a strut size of 1.0, the percentage of the organic phase was reduced from 64.6% to 58.1%, which translates to approximately 33% of PCL degradation over the course of 180 days, confirming the biodegradable nature of the copolymers and the slow degradation rates reported for PCL.

Similar data were collected for scaffolds prepared with PCL29 and a strut size of 0.8, where the percentage of the organic phase was reduced from 64.6% to 59%. The difference between the scaffolds prepared the two different strut sizes is attributed to the size of the pore channels, however the results suggests that the pore size does not play a very important role

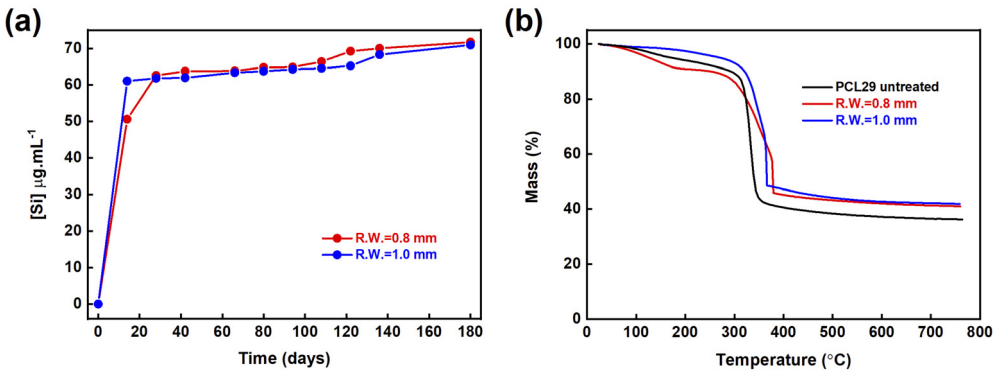


Fig. 7 (a) Si release of PCL29 (organic/inorganic: 70/30) 3D printed scaffolds (Strut size 0.8 mm and 1.0 mm) in PBS as a function of time, over the course of 180 days (ICP), (b) TGA graphs of PCL29 (organic/inorganic: 70/30) 3D printed scaffolds (Strut size 0.8 mm and 1.0 mm) after the exposure to PBS.

Open Access Article. Published on 27 August 2025. Downloaded on 10/3/2025 4:51:24 PM.
This article is licensed under a Creative Commons Attribution 3.0 Unported Licence.

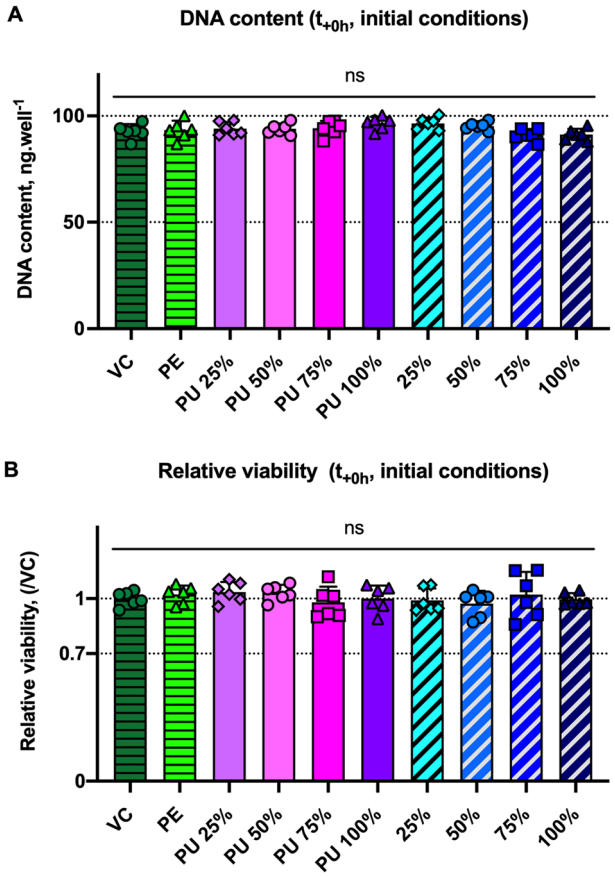


Fig. 8 Validation of initial conditions prior to *in vitro* cytotoxicity of dissolution products from different molar ratio of organic/inorganic PCL29 hybrids on h-BMSCs (1×10^4 cells per well on TCP, $n = 6$, $N = 1$): (A) DNA content in culture well representative of adherent h-BMSCs just prior to the *in vitro* cytotoxicity test. DNA content was estimated by reading the fluorescence intensity of Quanti-IT PicoGreen dye at an excitation wavelength of 480 ± 9 nm and an emission wavelength of 520 ± 15 nm; (B) relative cell viability in h-BMSCs just prior to exposure to conditioned media. A non-parametric Kruskal–Wallis multiple comparisons test was used to detect statistical significance between all conditions, ns $p > 0.05$, *$p < 0.1$ (h-BMSCs = human-bone marrow stromal cells).

as far as the biodegradation is concerned, as the margin is negligible.

The released silicon is likely to be in the form of orthosilicic acid ($Si(OH)_4$), generated *via* hydrolysis of surface silanol groups and minimal degradation of the covalent silica network.[55] The initial rapid release (~60 μg mL^{-1} within the first 10 days) aligns with dissolution of the silica surface, which is likely to have reduced connectivity, while the subsequent plateau reflects the stability of the bulk silica network. This behavior is consistent with Class II hybrids, where Si release occurs *via* hydrolytic dissolution rather than leaching of unreacted precursors.[6,7,55]

In vitro cytotoxicity

$Sn(Oct)_2$ was used as catalyst and it is essential to mention that as it is a metal-based catalyst, it is possible that trace amounts may remain in the polymer following synthesis. Residual $Sn(Oct)_2$ could potentially influence the thermal, mechanical, or degradation properties of the polymer, as well as its biocompatibility.[56–58] While no direct measurement of residual tin was performed in this study, all biological tests were carried

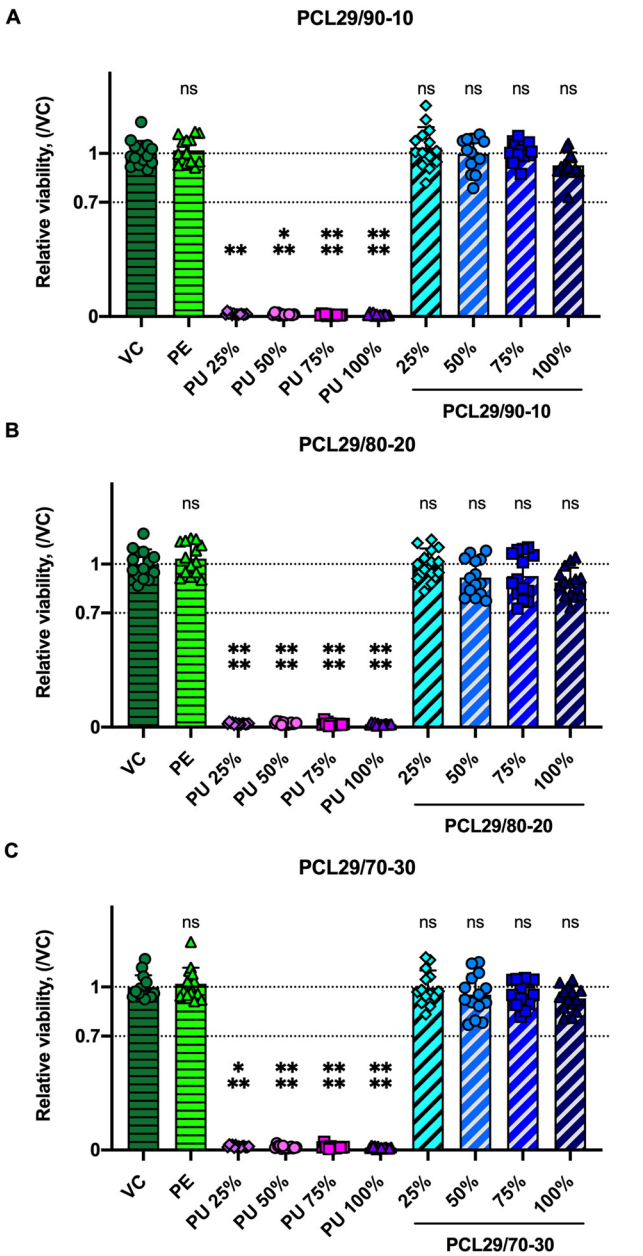


Fig. 9 Test for *in vitro* cytotoxicity of dissolution products from different molar ratio of organic/inorganic PCL29 hybrids on h-BMSCs as per ISO10993-5 and ISO10993-12 (1×10^4 cells per well on TCP, $n \geq 6$, $N \geq 2$). (A) Relative cell viability in h-BMSCs post-exposure to PCL29/90-10, (B) to PCL29/80-20, and (C) PCL29/70-30 hybrid disk conditioned media. The h-BMSC metabolic activity was assessed *via* MTT dye absorbance readings at 570 ± 15 nm wavelength. High density polyethylene (PE) film was used as negative control (reproducible non-cytotoxic) and polyurethane (PU) was used as positive control (reproducible cytotoxic). A non-parametric Kruskal–Wallis multiple comparisons test was used to detect statistical significance between conditions and the VC control samples, ns $p > 0.05$, **$p < 0.01$, ***$p < 0.001$, ****$p < 0.0001$ (h-BMSCs = human-bone marrow stromal cells).

This journal is © The Royal Society of Chemistry 2025

Open Access Article. Published on 27 August 2025. Downloaded on 10/3/2025 4:51:24 PM.
This article is licensed under a Creative Commons Attribution 3.0 Unported Licence.

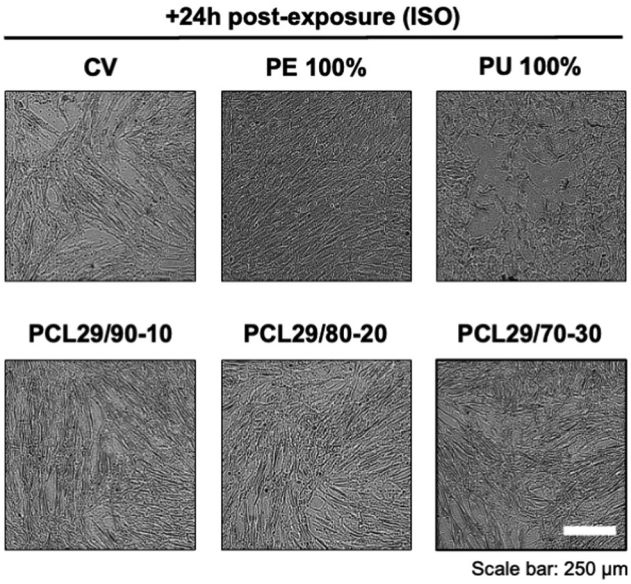


Fig. 10 Test for *in vitro* cytotoxicity of PCL29 hybrid dissolution products on h-BMSCs, as per ISO10993-5 and ISO10993-12. Representative bright-field micrographs of h-BMSCs post-exposure (+24 h) to basal control medium (vehicle, VC) or conditioned media with PU, PE or PCL29/70-30, PCL29/80-20 or PCL29/90-10 (1×10^4 cells per well on TCP, $n \geq 6$, $N \geq 2$). The micrographs were taken on a JuLI™ Stage Real-Time Cell History Recorder (NanoEnTek Inc., Korea).

out in accordance with ISO 10993 standards. *In vitro* cytotoxicity tests were conducted as per ISO 10993-5 by exposing h-BMSCs to media conditioned with the dissolution products of PCL29 hybrids with organic/inorganic molar ratios up to 70/30 for a period of 24 h. No significant differences between sample initial conditions were confirmed before the tests by measuring DNA content as representative of cell density and relative viability (Fig. 8(A) and (B)). Twenty-four hours post-exposure to PCL29 extracts, the viability in h-BMSCs exposed to PCL29/70-30, PCL29/80-20, and PCL29/90-10 extracts was consistently above the 70% ISO threshold defined by the basal and negative control samples (Fig. 9). No adverse cytotoxicity or changes in cell phenotype were observed *in vitro*, indicating that the purification protocol was effective under the conditions tested.

In parallel with the *in vitro* cytotoxicity tests, the samples were also live-monitored under a JuLI-stage live image phase contrast microscope to identify changes in cellular morphology post-exposure to the conditioned media. There was not any qualitative change in cell phenotype and cell growth due to the cytotoxic effects of PCL29/70-30, PCL29/80-20 and PCL29/90-10 extracts (Fig. 10).

The above-stated results indicate that the dissolution products of PCL29 hybrids with organic/inorganic molar ratios up to 70/30 do not induce acute effects on cell survival and metabolic activity and therefore the hybrids are biocompatible.

Conclusions

Silica/PCL-*b*-P(MMA-*co*-TMSPMA) hybrids were successfully produced using PCL-*b*-P(MMA-*co*-TMSPMA) copolymer synthesized with a combination of ROP and RAFT polymerization techniques, using PCL as a RAFT agent. The effect of the ratio of CL/silane containing units on the mechanical properties of the hybrids was investigated and it was demonstrated that the yield stress was higher for hybrids with the lowest CL/silane ratio, indicating that hybrids with tailored mechanical properties can be produced by varying the PCL content of the copolymers. The compositions with optimal mechanical properties in bulk form (yield stress 39.3 MPa to 52.9 MPa, yield strain 4–6%) were developed into "inks" for 3D printing and porous biodegradable scaffolds were successfully produced by direct writing. The mechanical properties of scaffolds with pore channels of 234–380 μm reduced yield strength to 5.2–7.4 MPa (dependent on copolymer and strut size used), but yield strain remained at ~4%. *In vitro* studies indicated biocompatibility, in terms of exposure of human bone marrow stem cells (hBMCs) to the dissolution products of the scaffolds, which contained silica species.

Author contributions

The manuscript was written through contributions of all authors. All authors have given approval to the final version of the manuscript.

Conflicts of interest

There are no conflicts to declare.

Data availability

Data for this article are available at Zenodo at **https://doi.org/10.5281/zenodo.14199284**.

Supplementary information is available that contains the ^{1}H-NMR spectra of CPAD, PCL, and PCL-CPAD macro-RAFT agent (Fig. S1), See DOI: **https://doi.org/10.1039/d5tb00220f**

Acknowledgements

The authors acknowledge the EPSRC (EP/S025782/1).

References

1 L. L. Hench and J. R. Jones, *Front. Bioeng. Biotechnol.*, 2015, **3**, 1–12.
2 E. M. Valliant and J. R. Jones, *Soft Matter*, 2011, **7**, 5083–5095.
3 Y. Shirosaki, Y. Yuki, T. Nakamura and A. Ohtsuki, in *Handbook of Sol-Gel Science and Technology: Processing, Characterization and Applications*, ed. L. C. Klein, M. Aparicio and A. Jitianu, Springer International Publishing, Cham, 2018, pp. 3619–3703.
4 J. Wen and G. L. Wilkes, *Chem. Mater.*, 1996, **8**, 1667–1681.
5 S. Pandey and S. B. Mishra, *J. Sol-Gel Sci. Technol.*, 2011, **59**, 73–94.

Open Access Article. Published on 27 August 2025. Downloaded on 10/3/2025 4:51:24 PM. This article is licensed under a Creative Commons Attribution 3.0 Unported Licence.

6 M. Nikshitha, S. M. Sudhakara and M. S. Shetty, *Mater. Chem. Phys.*, 2025, **331**, 130181.
7 J.-M. García-Martínez and E. P. Collar, *Polymers*, 2024, **16**(21), DOI: 10.3390/polym16213043.
8 J. R. Jones, *Acta Biomater.*, 2015, **23**, S53–S82.
9 S.-H. Rhee, J.-Y. Choi and H.-M. Kim, *Biomaterials*, 2002, **23**, 4915–4921.
10 S.-H. Rhee, Y.-K. Lee, B.-S. Lim, J. J. Yoo and H. J. Kim, *Biomacromolecules*, 2004, **5**, 1575–1579.
11 Y. Shirosaki, T. Okabayashi and S. Yasutomi, *Molecules*, 2020, **25**(22), DOI: 10.3390/molecules25225292.
12 Y. Shirosaki, T. Okayama, K. Tsuru, S. Hayakawa and A. Osaka, *Chem. Eng. J.*, 2008, **137**, 122–128.
13 Y. Shirosaki, K. Tsuru, S. Hayakawa, A. Osaka, M. A. Lopes, J. D. Santos and M. H. Fernandes, *Biomaterials*, 2005, **26**, 485–493.
14 C.-P. Li, M.-C. Weng and S.-L. Huang, *Polymers*, 2020, **12**(6), 1326.
15 Y.-C. Lin, H.-Y. Wang, Y.-C. Tang, W.-R. Lin, C.-L. Tseng, C.-C. Hu and R.-J. Chung, *Int. J. Biol. Macromol.*, 2024, **258**, 128845.
16 O. Mahony, O. Tsigkou, C. Ionescu, C. Minelli, L. Ling, R. Hanly, M. E. Smith, M. M. Stevens and J. R. Jones, *Adv. Funct. Mater.*, 2010, **20**, 3835–3845.
17 L. Ren, K. Tsuru, S. Hayakawa and A. Osaka, *Biomaterials*, 2002, **23**, 4765–4773.
18 G. Poologasundarampillai, C. Ionescu, O. Tsigkou, M. Murugesan, R. G. Hill, M. M. Stevens, J. V. Hanna, M. E. Smith and J. R. Jones, *J. Mater. Chem.*, 2010, **20**, 8952–8961.
19 G. Poologasundarampillai, B. Yu, O. Tsigkou, E. Valliant, S. Yue, P. D. Lee, R. W. Hamilton, M. M. Stevens, T. Kasuga and J. R. Jones, *Soft Matter*, 2012, **8**, 4822–4832.
20 L. S. Connell, L. Gabrielli, O. Mahony, L. Russo, L. Cipolla and J. R. Jones, *Polym. Chem.*, 2017, **8**, 1095–1103.
21 L. Gabrielli, L. Connell, L. Russo, J. Jiménez-Barbero, F. Nicotra, L. Cipolla and J. R. Jones, *RSC Adv.*, 2014, **4**, 1841–1848.
22 F. Tallia, L. Russo, S. Li, A. L. H. Orrin, X. Shi, S. Chen, J. A. M. Steele, S. Meille, J. Chevalier, P. D. Lee, M. M. Stevens, L. Cipolla and J. R. Jones, *Mater. Horiz.*, 2018, **5**, 849–860.
23 A. L. B. Maçon, S. J. Page, J. J. Chung, N. Amdursky, M. M. Stevens, J. V. M. Weaver, J. V. Hanna and J. R. Jones, *Phys. Chem. Chem. Phys.*, 2015, **17**, 29124–29133.
24 R. Ravarian, H. Wei, A. Rawal, J. Hook, W. Chrzanowski and F. Dehghani, *J. Mater. Chem. B*, 2013, **1**, 1835–1845.
25 R. Ravarian, X. Zhong, M. Barbeck, S. Ghanaati, C. J. Kirkpatrick, C. M. Murphy, A. Schindeler, W. Chrzanowski and F. Dehghani, *ACS Nano*, 2013, **7**, 8469–8483.
26 K.-H. Lee and S.-H. Rhee, *Biomaterials*, 2009, **30**, 3444–3449.
27 S.-H. Rhee, M.-H. Hwang, H.-J. Si and J.-Y. Choi, *Biomaterials*, 2003, **24**, 901–906.
28 A. L. B. Maçon, S. Li, J. J. Chung, A. Nommeots-Nomm, A. K. Solanki, M. M. Stevens and J. R. Jones, *J. Mater. Chem. B*, 2016, **4**, 6032–6042.
29 J. J. Chung, S. Li, M. M. Stevens, T. K. Georgiou and J. R. Jones, *Chem. Mater.*, 2016, **28**, 6127–6135.
30 J. M. Ren, T. G. McKenzie, Q. Fu, E. H. H. Wong, J. Xu, Z. An, S. Shanmugam, T. P. Davis, C. Boyer and G. G. Qiao, *Chem. Rev.*, 2016, **116**, 6743–6836.
31 A. Skandalis, T. Sentoukas, D. Giaouzi, M. Kafetzi and S. Pispas, *Polymers*, 2021, **13**(11), 1698.
32 A. Skandalis and S. Pispas, *J. Polym. Sci., Part A: Polym. Chem.*, 2019, **57**, 1771–1783.
33 A. Li Volsi, F. Tallia, H. Iqbal, T. K. Georgiou and J. R. Jones, *Mater. Adv.*, 2020, **1**, 3189–3199.
34 S. Perrier, *Macromolecules*, 2017, **50**, 7433–7447.
35 K. Hakobyan, F. Ishizuka, N. Corrigan, J. Xu, P. B. Zetterlund, S. W. Prescott and C. Boyer, *Adv. Mater.*, 2025, **37**, 2412407.
36 G. Moad, E. Rizzardo and S. H. Thang, *Aust. J. Chem.*, 2012, **65**, 985–1076.
37 J. J. Chung, J. Yoo, B. S. T. Sum, S. Li, S. Lee, T. H. Kim, Z. Li, M. M. Stevens, T. K. Georgiou, Y. Jung and J. R. Jones, *Adv. Healthcare Mater.*, 2021, **10**, 2100117.
38 J. J. Chung, Y. Fujita, S. Li, M. M. Stevens, T. Kasuga, T. K. Georgiou and J. R. Jones, *Acta Biomater.*, 2017, **54**, 411–418.
39 S. G. Krimmer, H. Pan, J. Liu, J. Yang and J. Kopeček, *Macromol. Biosci.*, 2011, **11**, 1041–1051.
40 J. Akimoto, M. Nakayama, K. Sakai, M. Yamato and T. Okano, *Polym. J.*, 2013, **45**, 233–237.
41 M. Doube, M. M. Kłosowski, I. Arganda-Carreras, F. P. Cordelières, R. P. Dougherty, J. S. Jackson, B. Schmid, J. R. Hutchinson and S. J. Shefelbine, *Bone*, 2010, **47**, 1076–1079.
42 H. Kakwere and S. Perrier, *J. Polym. Sci., Part A: Polym. Chem.*, 2009, **47**, 6396–6408.
43 U. Capasso Palmiero, M. Sponchioni, N. Manfredini, M. Maraldi and D. Moscatelli, *Polym. Chem.*, 2018, **9**, 4084–4099.
44 J. J. Chung, B. S. T. Sum, S. Li, M. M. Stevens, T. K. Georgiou and J. R. Jones, *Macromol. Rapid Commun.*, 2017, **38**, 1700168.
45 J. J. Chung, S. Li, M. M. Stevens, T. K. Georgiou and J. R. Jones, *Chem. Mater.*, 2016, **28**, 6127–6135.
46 R. M. Aspden, in *Bone Research Protocols*, ed. S. H. Helfrich Miep and H. Ralston, Humana Press, Totowa, NJ, 2003, pp. 369–379.
47 A. Heyraud, F. Tallia, D. Sory, H.-K. Ting, A. Tchorzewska, J. Liu, H. L. Pilsworth, P. D. Lee, J. V. Hanna, S. M. Rankin and J. R. Jones, *Front. Bioeng. Biotechnol.*, 2023, **11**, DOI: 10.3389/fbioe.2023.1224596.
48 R. C. Atwood, J. R. Jones, P. D. Lee and L. L. Hench, *Scr. Mater.*, 2004, **51**, 1029–1033, DOI: 10.1016/j.scriptamat.2004.08.014.
49 J. R. Jones, P. D. Lee and L. L. Hench, *Philos. Trans. R. Soc., A*, 2006, **364**, 263–281, DOI: 10.1098/rsta.2005.1689.
50 J. R. Jones, R. C. Atwood, G. Poologasundarampillai, S. Yue and P. D. Lee, *J. Mater. Sci.: Mater. Med.*, 2009, **20**, 1404–1413.
51 S. Yue, P. D. Lee, G. Poologasundarampillai, Z. Yao, P. Rockett, A. H. Devlin, C. A. Mitchell, M. A. Konerding and J. R. Jones, *J. Mater. Sci.: Mater. Med.*, 2010, **21**, 847–853.
52 X. Yuan, T. Wu, T. Lu and J. Ye, *J. Mater. Sci.: Mater. Med.*, 2024, **35**, 54.

 This journal is © The Royal Society of Chemistry 2025

53 T. Lu, G. Li, L. Zhang, X. Yuan, T. Wu and J. Ye, *Mater. Today Bio*, 2024, **28**, 101203.
54 M. Bartnikowski, T. R. Dargaville, S. Ivanovski and D. W. Hutmacher, *Prog. Polym. Sci.*, 2019, **96**, 1–20, DOI: **10.1016/j.progpolymsci.2019.05.004**.
55 S. Mohanan, X. Guan, M. Liang, A. Karakoti and A. Vinu, *Small*, 2024, **20**, 2301113.
56 G. Rokicki and P. G. Parzuchowski, in *Polymer Science: A Comprehensive Reference*, ed. K. Matyjaszewski and M. Möller, Elsevier, Amsterdam, 2012, pp. 247–308.
57 H. Nishida, T. Mori, S. Hoshihara, Y. Fan, Y. Shirai and T. Endo, *Polym. Degrad. Stab.*, 2003, **81**, 515–523.
58 P. S. Giram and B. Garnaik, *Polym. Adv. Technol.*, 2021, **32**, 4502–4515.

Open Access Article. Published on 27 August 2025. Downloaded on 10/3/2025 4:51:24 PM.
This article is licensed under a Creative Commons Attribution 3.0 Unported Licence.